ADVANCED THEORY AND SIMULATIONS
www.advtheorysimul.com

Aerodynamic and Acoustic Simulations of Thick Flatback Airfoils Employing High Order DES Methods

Galih Bangga, Ferdinand Seel, Thorsten Lutz, and Timo Kühn*

The results of high fidelity aerodynamic and acoustic computations of thick flatback airfoils are reported in the present paper. The studies are conducted on a flatback airfoil having a relative thickness of 30% with the blunt trailing edge thickness of 10% relative to chord. Delayed Detached-Eddy Simulation (DDES) approaches in combination with high order (5th) flux discretization WENO (Weighted Essentially Non-Oscillatory) and l^2*Roe* Riemann solver are employed. Two variants of the DES length scale calculation methods are compared. The results are validated against experimental data with good accuracy. The studies provide guideline on the mesh and turbulence modeling selection for flatback airfoil simulations. The results indicate that the wake breakdown is strongly influenced by the spanwise resolution of the mesh, which directly contributes to the prediction accuracy especially for drag force and noise emission. The Reynolds normal stress $\overline{u'u'}$ and the $\overline{u'v'}$ Reynolds stress component have the largest contributions on the mixing process, while the contribution of the $\overline{u'w'}$ component is minimal. Proper orthogonal decomposition is further performed to gain deeper insights into the wake characteristics.

1. Introduction

Wind energy development grows significantly in the last decade due to surged people consciousness toward clean energy production and due to the increased cost competitiveness to fossil fuel sources. Data show that most of today's wind turbine power are generated onshore.[1] In contrast, available sites with high wind potential are inherently limited. Repowering is often chosen as the solution,[2] by replacing old turbines with newer and larger turbines having higher power production. The increased turbine size enforces blade designers to adopt much thicker airfoils than the classical turbine blades for a significant portion of the blade radius.[3]

It is well known in wind turbine community that thick airfoils have poorer aerodynamic performance than thin airfoils. This has been reported for instance in ref. [4–13]. The shape of these airfoils have stronger adverse pressure gradient than thin airfoils, and hence promotes stronger flow separation. Moreover, the leading edge of the blade sections cannot be avoided from contamination from bugs or dirt during wind turbine operation, and this could potentially lead to premature laminar to turbulent transition of the flow over the aerodynamic profiles. Measurements reported by Timmer and Rooij,[4,5] Ehrmann et al.,[10] and Wilcox et al.[12] demonstrate that the maximum lift coefficient and global aerodynamic performance under such conditions are worse than those measured for the same airfoils/blade sections having clean conditions. Furthermore, stall occurs earlier and its characteristic is less favorable. This becomes a great challenge for blade designers to reduce the sensitivity of the airfoil toward surface roughness near the leading edge.

To overcome this limitation and to increase the structural strength at the same time, flatback airfoils are introduced in the root area of wind turbine blades. Flatback airfoils are created by enlarging the trailing edge thickness and redistributing the shape of the airfoil for a certain proportion along the chordwise direction. This reduces the adverse pressure gradient and as a consequence promotes aerodynamic performance improvement. Studies[14–21] have shown that the maximum achievable lift coefficient and lift curve slope could be enhanced by adopting the flatback airfoil concept. Furthermore, the sensitivity of the lift and drag characteristics to surface soiling effects is also reduced.[16,17]

Despite the promising advantages of flatback airfoil, it has its own drawbacks. The flow in the wake of the airfoil becomes unsteady due to the increased trailing edge thickness, even at zero angle of incidence. The blunt trailing edge generates counter-rotating vortices detaching periodically from the upper and lower edge of the base.[20] This evokes fluctuations of the forces acting on the airfoil and increased noise tonality at relatively low frequency domain.[22] This is clearly not desirable and should be

G. Bangga[+], F. Seel, T. Lutz
University of Stuttgart
Institute of Aerodynamics and Gas Dynamics (IAG)
70569 Stuttgart, Germany
E-mail: bangga@iag.uni-stuttgart.de; galih.bangga@dnv.com
T. Kühn
Wobben Research and Development GmbH (WRD)
26607 Aurich, Germany

The ORCID identification number(s) for the author(s) of this article can be found under https://doi.org/10.1002/adts.202200129

[+]Present address: DNV Services UK, One Linear Park, Avon Street, Temple Quay, Bristol BS2 0PS, United Kingdom

DOI: 10.1002/adts.202200129

avoided for designing a wind turbine blade. Despite that, there is only limited knowledge in this area due to the complexity of the case and its difficulty to be computed numerically, even when high fidelity computational fluid dynamics (CFD) codes were employed.[16,18–20,23–27] Stone et al.[23] demonstrated that the prediction of drag coefficient varies significantly depending on the employed codes and computational meshes. Furthermore, most studies were focused on the force assessments but little effort has been spent for wake analysis.[16,18–20,23–27] On the other hand, further evaluating the wake flow characteristics is needed to understand the flow physics because the forces acting on the airfoil and the noise emission are dominated by the flow fluctuations in the wake.

From the above discussions, it can be seen that there are still gaps concerning a complete understanding of the interactions between the unsteady characteristics of wake with the resulting forces and noise emission of flatback airfoils. The present studies are aimed at investigating these effects with the help of high fidelity computational approaches. First of all, the influences of numerical setup on the aerodynamic and acoustic characteristics of flatback airfoils shall be evaluated to gain a solid basis for the evaluation process. Deeper analyses into the wake flow characteristics and flow field decomposition using the proper orthogonal decomposition (POD) will be performed. The connections with the solution accuracy and the generated noise as well as resulting forces will be identified. The main novelty of the paper is in the comprehensive evaluations of the flatback airfoil forces and noise in relations with the wake characteristics and model reduction by means of POD. At present, no literature was dedicated to account for such combined studies for flatback airfoils at wind turbine relevant Reynolds number. The obtained results may serve as a basis in designing an efficient noise control strategy for flatback airfoils.

The present paper is constructed as follows. Section 2 presents the employed computational approach and test case. The results of the computational studies will be presented in Section 3 in terms of the numerical setup effects, wake characeristics and flow decomposition. Finally, all results will be concluded in Section 4.

2. Computational Setup

2.1. Airfoil and Flow Conditions

The studies were conducted on a flatback version of the DU 97 W-300 airfoil with a 30% relative thickness. Measurements were done for this airfoil at the Sandia National Laboratory in the Virginia Tech stability wind tunnel.[21] The chord length of the airfoil was 0.914 m spanning up to 1.8 m in the wind tunnel. The airfoil was measured under clean and tripped (at 5% suction side and 10% pressure side) conditions in terms of lift, drag, and acoustic emission. The acoustic measurements were conducted using a 63-microphone phased array with a center being aligned with the airfoil center of rotation having a distance of 3.04 m in vertical direction. In the present studies, the measured cases having a wind speed of about 57 m s^{-1} were considered.[21] This corresponded to a Reynolds number of 3.2 million and was the largest tested velocity in the measurement campaign. Three different angles of attack (α) were taken into account: 5.1°, 12.8°, and 15.4°.

2.2. Computational Fluid Dynamics

The CFD computations in the present studies were carried out using a CFD code FLOWer. The code solved the compressible Navier-Stokes equations applying a finite volume formulation on a block-structured mesh. The basic version of the code was developed by the German Aerospace Center (DLR).[28] The FLOWer code was continuously extended by the Institute of Aerodynamics and Gas Dynamics (IAG) at the University of Stuttgart for the simulations of wind turbine components, including the usages of high fidelity eddy resolving computations and high order flux discretizations.[29–31] The code made use of a central space discretization with artificial dissipation being calculated in relation to the grid cell aspect ratio.[32] This approach was robust and well suited for parallel application.[32] Furthermore, the time integration for the unsteady calculations was conducted under the use of an explicit 5-stage Runge-Kutta scheme, which can be accelerated by methods of local time stepping, resulting in a second order accuracy in time. The time step applied is defined by $\Delta t = c/(100 \cdot U_\infty)$, with c and U_∞ being the airfoil chord and undisturbed inflow velocity, respectively. The multigrid level 3 was further used to accelerate convergence.[33]

The FLOWer code supported the usage of the overlapping mesh (chimera) technique. This allowed several grid components to be built independently, making the grid generation process easier without sacrificing the accuracy and quality of the mesh. In the present studies, the computational grid consisted of two main components, namely background (black color) and airfoil meshes (red color) as shown in **Figure 1**. The background domain was large enough ($> 100c$) to contain the wake in all directions. The grid adopted a nonconformal (hanging-grid) fully structured mesh approach to save the computational expenses and to enable the usages of high order flux discretization methods. This finest mesh resolution in the near wake region was $\Delta x = \Delta y = \Delta z = 0.01c$ that was suitable for eddy resolving computations. The cell size was subsequently increased until $\Delta x = \Delta y = \Delta z = 1c$ in the outer domain of the mesh.

The airfoil mesh was generated by an in-house automated script using Pointwise grid generator.[34] The grid adopted an *O*-type topology and was generated independent of the background mesh, and combined using the chimera approach. The chimera mesh approach accelerated the grid creation significantly while still maintaining the quality of the mesh. The mesh resolution in the chimera interpolation area was close to $0.01c$, similar with the background mesh resolution at the same location. The airfoil was discretized by 512 cells in circumferential direction (256 on pressure side + 256 on suction side) and 128 cells are allocated on the trailing edge base according to a past study.[20] To properly resolve the boundary layer, 64 cells were applied across the boundary layer domain with a growth rate of 1.07 and the first wall distance of the grid satisfies $y^+ < 1.0$. The normal direction of the airfoil mesh excluding the boundary layer domain was discretized by 144 grid cells. Detail of the meshes considered in the studies is given in **Table 1**. Three different 3D meshes were considered in the studies by changing the mesh resolution along the spanwise length of $0.5c$. This varies the cell size in z direction from $0.0078c$, $0.0052c$, to $0.0038c$. An illustration of this refinement effect on the mesh distribution on airfoil is shown in **Figure 2**. Additionally, a 2D version of the mesh is also considered

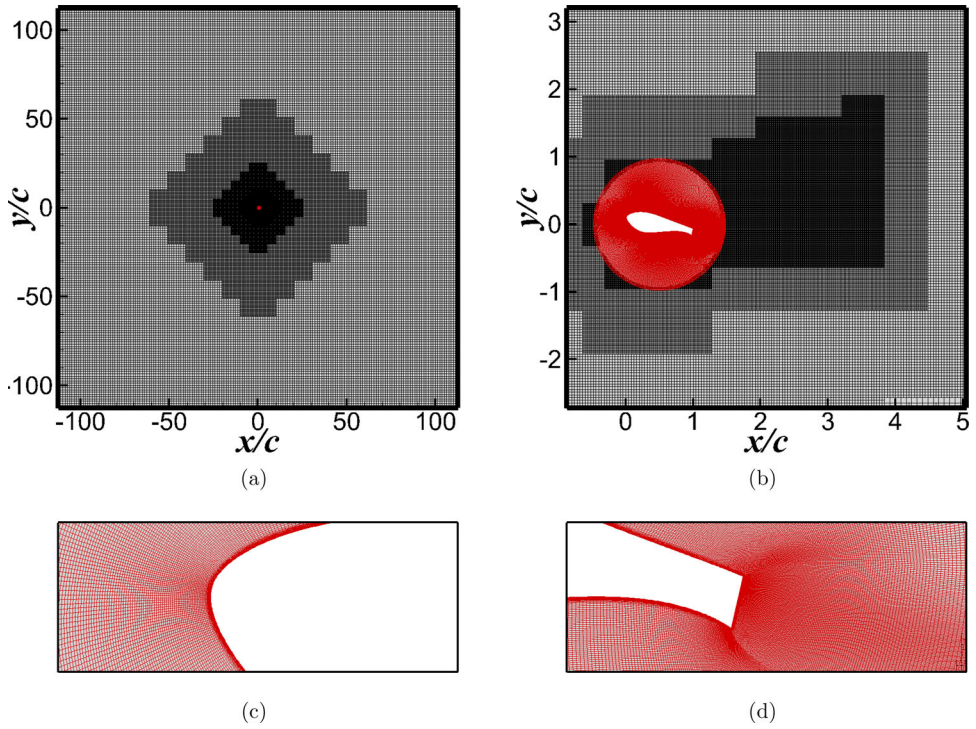

Figure 1. Detailed overview of the simulation domain and computational meshes.

Table 1. Computational grid parameters considered in the studies. PS: pressure side, SS: suction side.

Grid	SS cells $N_{\xi,SS}$	PS cells $N_{\xi,PS}$	TE cells N_{TE}	BL cells N_{BL}	Normal cells N_{η}	Span cells N_Z	Span length L_z/c
Grid C	256	256	128	64	144	64	0.5
Grid M	256	256	128	64	144	96	0.5
Grid F	256	256	128	64	144	128	0.5
Grid 2D	256	256	128	64	144	–	–
Grid F Short	256	256	128	64	144	64	0.25
Grid F Long	256	256	128	64	144	256	1.0

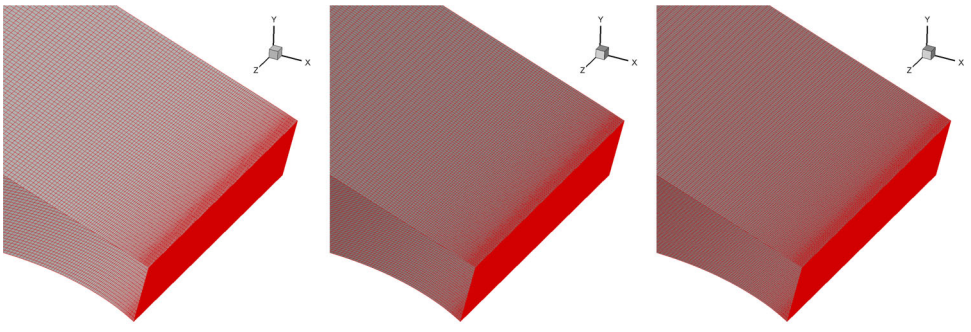

Figure 2. Mesh distribution on the airfoil surface for three different spanwise mesh resolution: a) $\Delta z = 0.0078c$, b) $\Delta z = 0.0052c$, and c) $\Delta z = 0.0038c$ which correspond to $N_Z = 64$, 96, and 128 cells, respectively.

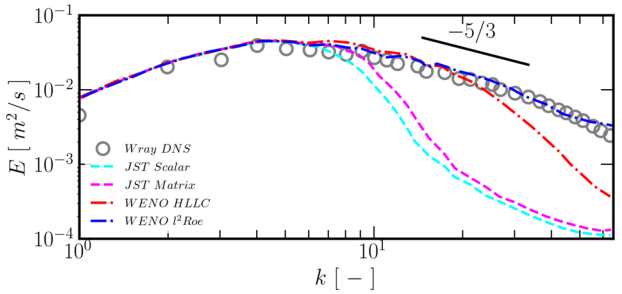

Figure 3. Energy spectra from NACA 0021 airfoil simulations at 60° incidence. The DNS data was obtained from [44] and all DES simulations were obtained from previous simulations in [29]. The WENO l^2*Roe* scheme was adopted in the present simulations.

to enable a comparison between 2D and 3D simulation environment. Also to study the influence of the simulated span length, the finest grid resolution was shorten to half and lengthen to double of the original span length. In that sense, the amount of the spanwise cells was adjusted accordingly. In all simulations, the angle of attack was changed by rotating the airfoil about its quarter chord location.

A high order (5th) WENO (Weighted Essentially Non-Oscillatory) scheme[35] for flux computation together with the l^2*Roe* Riemann solver was applied on the block background mesh component. The usage of central scheme-based WENO may provide a higher degree of accuracy instead of the upwind-based scheme as in ref. [35], e.g. those from ref. [36–38]. Despite that, it was observed from the previous studies that as long as a high enough order of the WENO scheme was adopted, the numerical dissipation can be minimized. Surely, providing that the spatial and temporal spacing requirements are met. The computational settings in the present studies were prepared according to the previous works for airfoil, helicopter wind turbine cases, e.g., ref. [29–31, 39–41]. In these studies, the employed WENO scheme was able to model the turbulent kinetic energy of the flow and the decay of atmospheric turbulence fairly well compared to reference data, as illustrated for the NACA 0021 airfoil simulation results at 60° incidence in **Figure 3**. The present computations were conducted employing an eddy resolving Delayed Detached-Eddy Simulation (DDES) approach.[29] The method ensures the turbulent structures of the separated flow to be resolved without relying on RANS models, except in the vicinity of the wall area where the SST $k-\omega$ model was applied.[42] Two variants of DES length scale calculation methods were considered, namely the standard maximum cell size method, $\Delta_{DES} = \max(\Delta x, \Delta y, \Delta z)$, and a newly implemented shear-layer adaptive (SLA) method.[41,43] Boundary layer transition was enforced at the same locations as in the experimental campaign.

2.3. Computational Aeroacoustics

To determine the noise emission toward an observer at a specific location in the farfield, an in-house CAA code ACCO[45] was employed in the studies. The code makes use of the Ffowcs Williams-Hawkings (FWH) equation for solving the nonlinear acoustic problems. The main basis of the CAA computations was the extracted time-dependent CFD solutions for a period of time. The data used for acoustic analysis was extracted at each time step of the CFD computations following convergence. The time-dependent CFD simulation variables over a prescribed surface f generated monopole and dipole sources. If the volume zone enclosing the surface was defined, quadrupole noise sources could be computed. Equation (1) shows the FWH equation being solved using ACCO. The right-hand side represents the source terms while the left-hand side is for the wave propagation.

$$\frac{\bar{\partial}^2\bar{\rho}'}{\partial t^2} - c^2\bar{\nabla}^2\rho' = \frac{\partial^2}{\partial x_i \partial x_j}[T_{ij}H(f)] - \frac{\partial}{\partial x_i}[(p'n_i + \rho u_i(u_n - v_n))\delta(f)] + \frac{\partial}{\partial t}[(\rho_0 v_n + \rho(u_n - v_n))\delta(f)] \quad (1)$$

with ρ' and p' being the fluctuations of density and pressure, respectively. The variable u_n and v_n represent the normal components of the fluid and surface velocities, respectively, δ is the Dirac delta function, T_{ij} is the Lighthill tensor and $H(f)$ is the Heavyside function of the integration surface function f. The flow outside of the integration surface was assumed to be at undisturbed state with the use of the left-hand side wave equation. The source terms on the right-hand side can be interpreted as volume displacement (monopoles), load fluctuations (dipoles) when the considered integration surface coincides with the physical surface itself. Compressibility effects were considered quadrupole noise sources.[40]

In the present studies, the physical blade surface itself was used as the integration surface for the FWH analysis. The quadrupole effects were neglected since the Mach number was very small in the test cases considered. The time accuracy was limited by the linear interpolation onto observer time slots, and especially by errors in the CFD input data. Those discrepancies between time step led to glitches in the pressure timeline solely by numerical artifacts. Those can be regarded as unwanted high-frequency components. To solve for this issue, filtering was applied to smooth out the data. By experience, a hundred runs of the fourth order filter yielded reasonably good solution.[46] Since it was too costly to simulate the whole airfoil span, the root mean square of the pressure sound (p_{rms}) was multiplied by the ratio of the real airfoil span to the simulated span (ζ) before the sound pressure level (SPL) is computed as:

$$SPL = 10\log_{10}\left(\frac{\zeta^2 p_{rms}^2}{p_{ref}^2}\right). \quad (2)$$

with p_{ref} defines the reference sound pressure of 2×10^{-5} Pa. For all calculations, the observer was located according to the experimental campaign, at $x = 0.25c$ and $y = 3.326c$ above the airfoil fixed in the inertial system.

3. Results and Discussion

3.1. Effects of Computational Grid

In this section, the effects of computational grid on the prediction accuracy in terms of the aerodynamic loads and acoustic

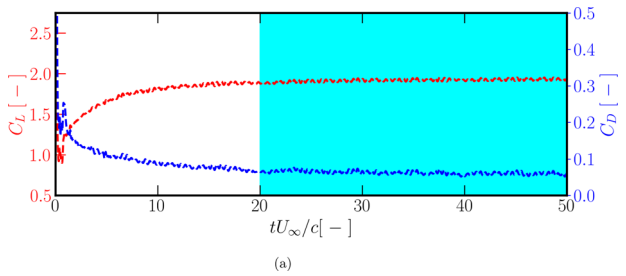

Figure 4. Convergence of the lift and drag coefficient monitored over the time. The data are evaluated once the desired convergence is achieved, presented by the shaded area.

emission will be assessed. As presented in Table 1, six different grids will be tested. The simulations were monitored over the time, and the evaluations of the results were carried out once the desired convergence of the lift and drag forces were obtained as illustrated in **Figure 4**. The comparison results are given in **Figure 5** in terms of the lift (C_L) and drag coefficients (C_D). Both clean and tripped measurement datasets are presented. Despite that, only the turbulent boundary layer results were considered in the CFD simulations. For comparison, measurement data of the sharp trailing edge version of the airfoil obtained from ref. [4] at a Reynolds number of 3 million is also given. It can be seen that flatback generally increases both lift and drag coefficients.

Figure 5 shows that the prediction of C_L is relatively independent of the spanwise grid resolution. One can see that the predicted lift is accurate for all tested 3D grids. Despite that, 2D calculations overestimate the predicted lift coefficient for the highest considered angle of attack of 15.4°. Drag prediction is more challenging than lift prediction as becomes evident in Figure 5. The coarsest spanwise resolution ($\Delta z = 0.0078c$) slightly overestimates drag. The results clearly indicate that the predicted drag no longer significantly changes from the medium grid ($\Delta z = 0.0052c$) to the fine grid ($\Delta z = 0.0038c$). This observation is interesting because the coarse grid is actually already fine enough for common DES computations. This is caused by the inability of the coarse mesh to simulate complex 3D mixing in the wake as will be further discussed in Section 3.4. As expected, the drag prediction using a full 2D approach is inaccurate since 3D effects are completely missing.

The prediction of the noise emission in **Figure 6** is also very challenging, similar to the drag prediction. It can be seen that the accuracy of the predicted noise increases with increasing number of spanwise cells. Medium and fine meshes yield similar results as the measured data, while the coarse grid tends to overestimate the aerodynamic noise. It also becomes clear that the 2D simulation environment is not suitable for the noise prediction of the studied case.

Figure 7 shows the influence of the spanwise length on the predicted aerodynamic and acoustic characteristics. All simulations employ the same spanwise cell size of $\Delta z = 0.0038c$. One can see that the prediction accuracy is relatively unaffected by the change. This implies that a shorter spanwise length of $0.25c$ will be sufficient for accurate predictions. This is beneficial because

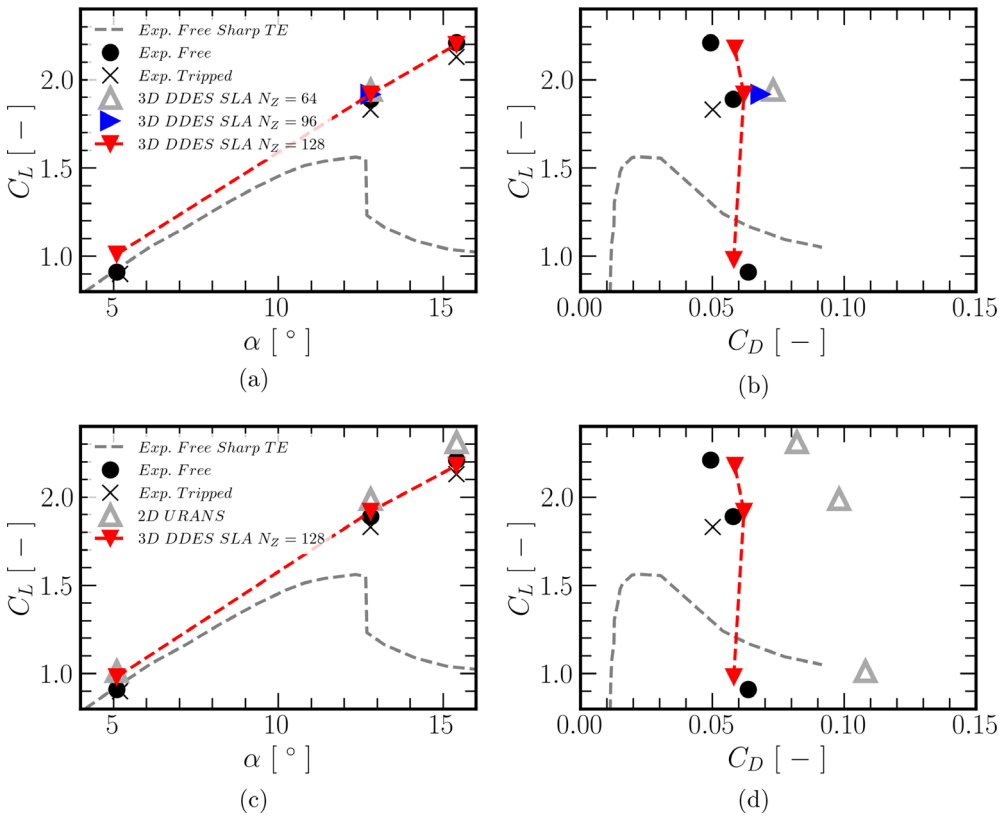

Figure 5. Aerodynamic forces predicted using four different grids. a,b) Effects of spanwise resolutions. c,d) Comparison between 2D and 3D simulations.

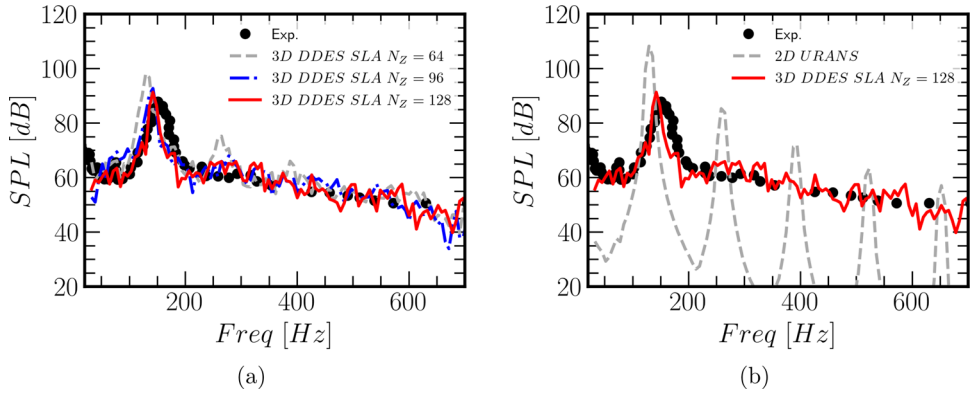

Figure 6. Aerodynamic noise predicted using four different grids at $\alpha = 12.8°$. a) Effects of spanwise resolutions. b) Comparison between 2D and 3D simulations.

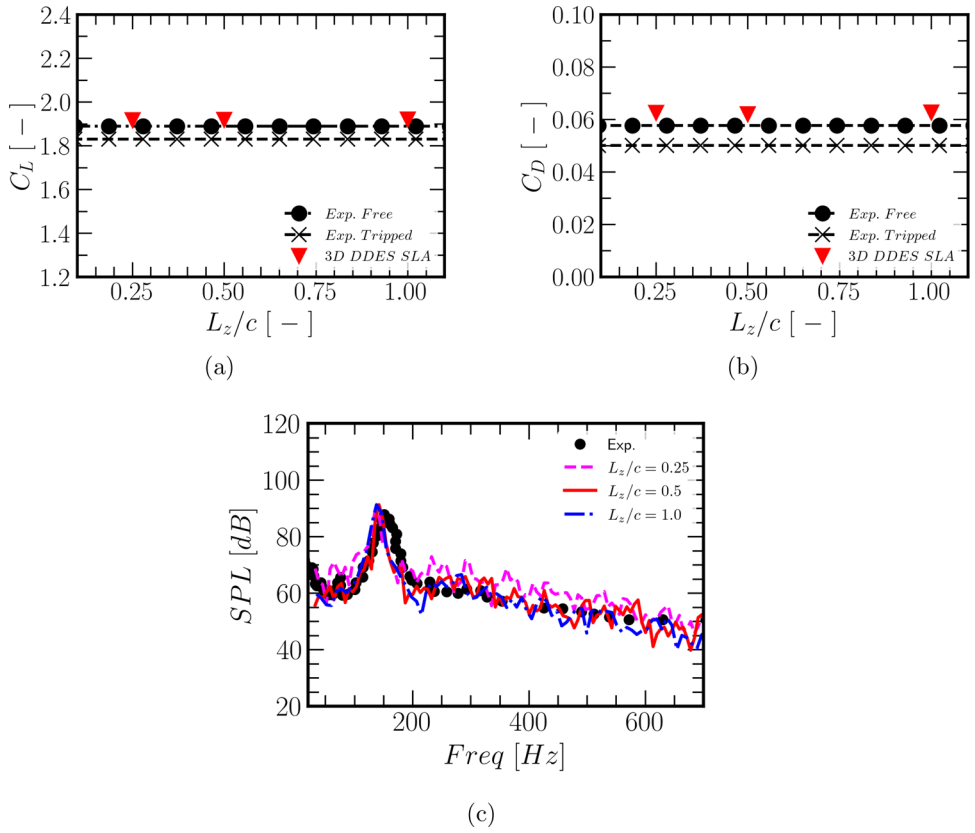

Figure 7. Aerodynamic forces and noise predicted using the fine grid resolution for three different spanwise distances.

this configuration costs only half of the computational effort for the case adopting $L_z/c = 0.5c$.

3.2. Effects of Employed Turbulence Model

This section discusses the influence of the employed turbulence model on the accuracy of the CFD simulations in terms of the aerodynamic and acoustic predictions. The computations employ the fine grid resolution (Grid F in Table 1). The URANS SST $k-\omega$ turbulence model is considered for the URANS computations. As the employed DES model also adopts the SST $k-\omega$ model in the wall bounded domain, separation location on the airfoil surface should be comparable for both cases. Thus, this section highlights the capability of the turbulence model to transport the separated wake downstream of the trailing edge which influences the force and noise predictions.

Figure 8 presents the aerodynamic forces predicted using 3D URANS and 3D DES. One can see that the lift coefficient is predicted by URANS fairly well, although it is slightly higher than the DES prediction. However, drag is again overestimated by URANS. The predicted drag level is even similar with the

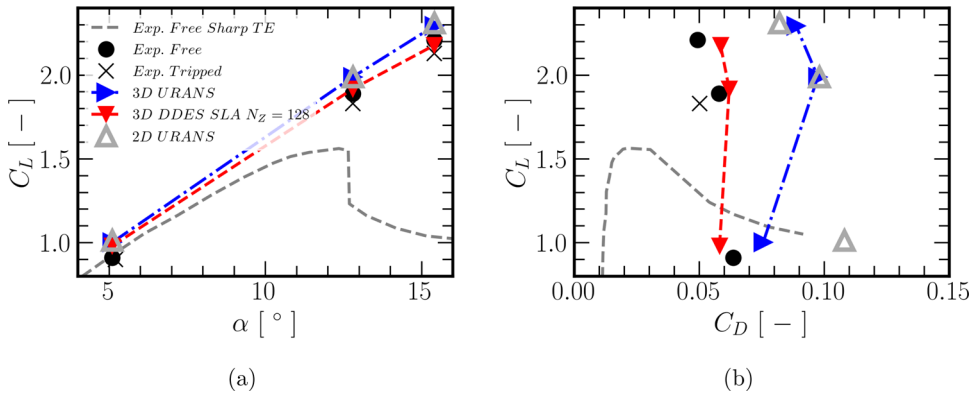

Figure 8. Aerodynamic forces predicted using two turbulence modeling approaches.

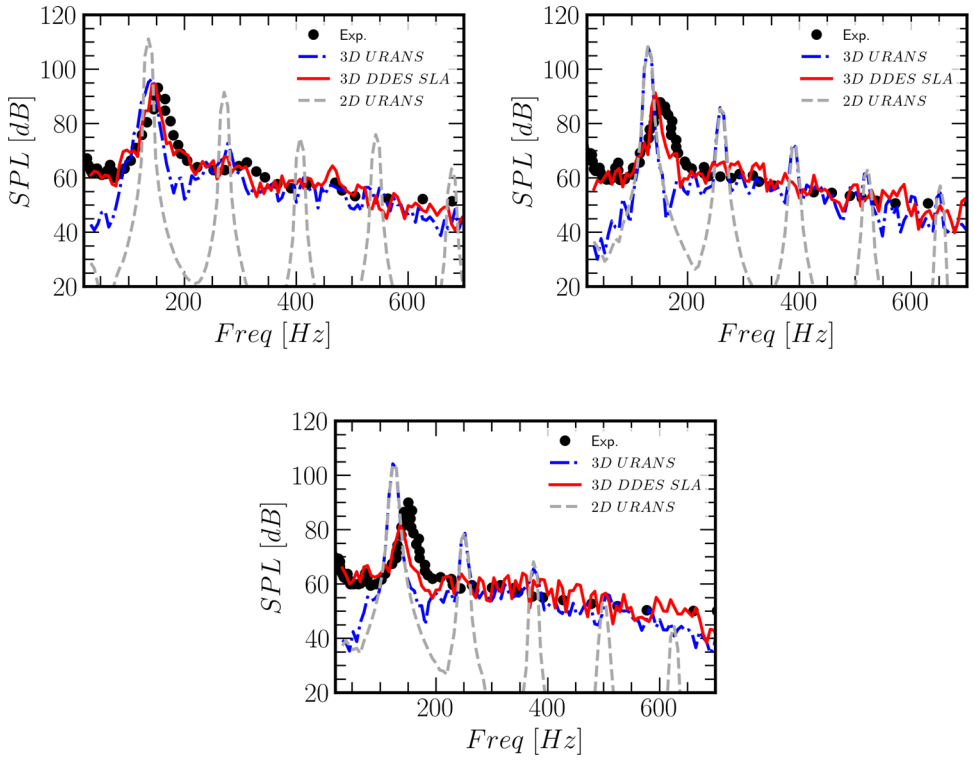

Figure 9. Aerodynamic noise predicted using two turbulence modeling approaches. a) $\alpha = 5.1°$, b) $\alpha = 12.8°$, and c) $\alpha = 15.4°$.

2D simulation results. In **Figure 9**, the acoustic emission of the airfoil is presented. As expected, URANS overestimates the noise prediction in comparison with the measured data and DES results. From the assessments, it can be inferred that drag prediction accuracy seems to be a good indication for the accuracy of the noise prediction results.

3.3. Effects of DES Length Scale Calculation Method

Two variants of DES length scale calculation methods, namely max($\Delta x, \Delta y, \Delta z$) and SLA, will be evaluated in this section. The latter is expected to be less severe to modeled stress depletion issue than the earlier. The computations employ the fine grid resolution (Grid F in Table 1). **Figure 10** displays the aerodynamic forces estimated using these two approaches. The prediction accuracy for both DES length scale calculation methods are very similar for the considered case, even for the drag force. This shows that modeled stress depletion is not a critical issue for the studied case. In fact, the location of flow separation is determined by the blunt trailing edge airfoil itself. Thus, separation is not driven by the pressure gradient.

Figure 11 presents the predicted aerodynamic noise for three different angles of attack, namely $\alpha = 5.1°$, $\alpha = 12.8°$, and $\alpha = 15.4°$. For the lowest considered angle of attack, the predicted noise spectra from both DES length scale calculation methods are similar for the whole considered frequency range. This result is consistent with the aerodynamic force

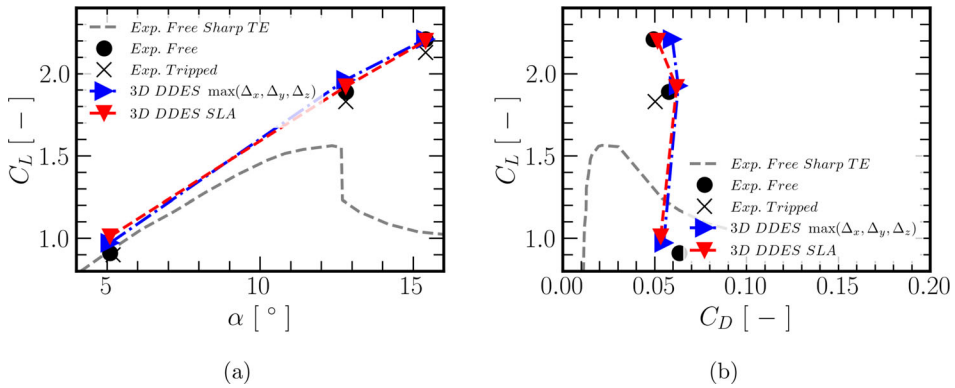

Figure 10. Aerodynamic forces predicted using two different DES length scale calculation methods.

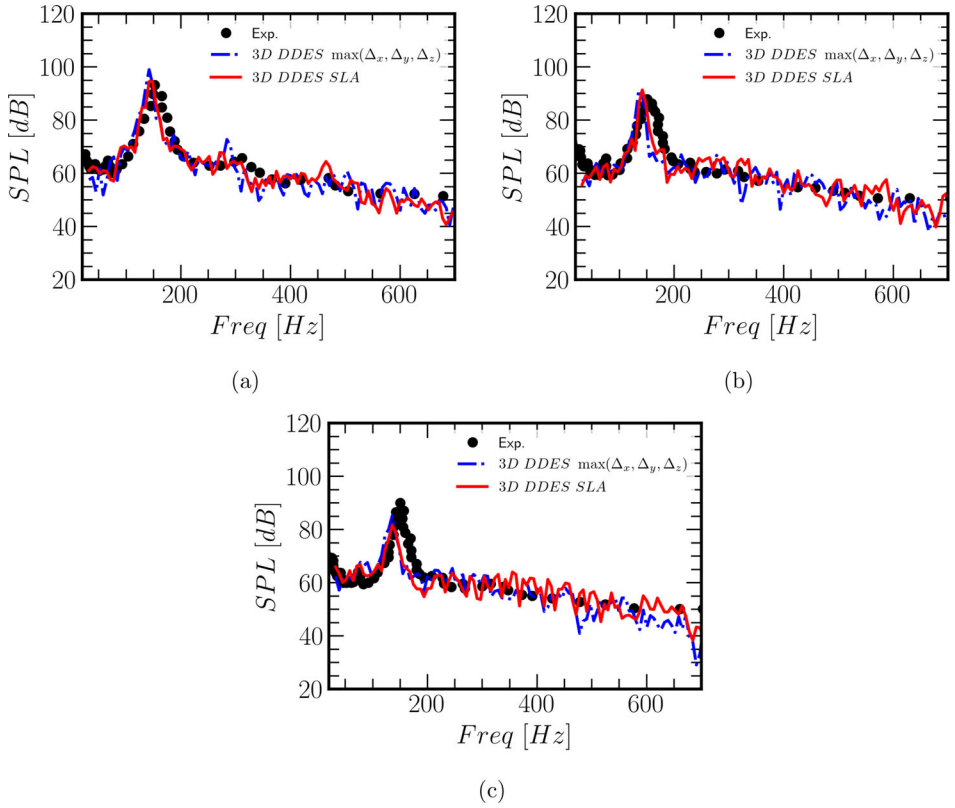

Figure 11. Aerodynamic noise predicted using two different DES length scale calculation methods. a) $\alpha = 5.1°$, b) $\alpha = 12.8°$, and c) $\alpha = 15.4°$.

prediction in Figure 10. For $\alpha = 12.8°$, a noticeable discrepancy is observed in the small frequency domain, where the peak of the noise spectra is shifted toward the lower frequency in the max($\Delta x, \Delta y, \Delta z$) method. This could possibly be caused by the limited simulated timeseries of the sound pressure. Despite that, longer simulations will be very expensive for DES computations. Nevertheless, these two methods agree for the rest of the frequency range fairly well. The highest considered angle of attack ($\alpha = 15.4°$) also demonstrates that both approaches yield similar results. This further confirms that the choice of DES length scale prediction method is not sensitive for flatback airfoil case as long as there is no premature separation in the trailing edge region.

Figure 12 shows the demarcation of the LES and RANS domains obtained from the DES computations at the same time instance. Although in general the behavior of both employed DES length scale calculation methods is similar, it can be seen that the SLA approach provides faster transition to LES within separated flow area, especially downstream the trailing edge base. The RANS area is remarkably suppressed for this approach. This may provide better separated flow characteristic predictions.

3.4. Wake Characteristics

In this section, the wake characteristics downstream of a flatback airfoil will be evaluated. The results were obtained from

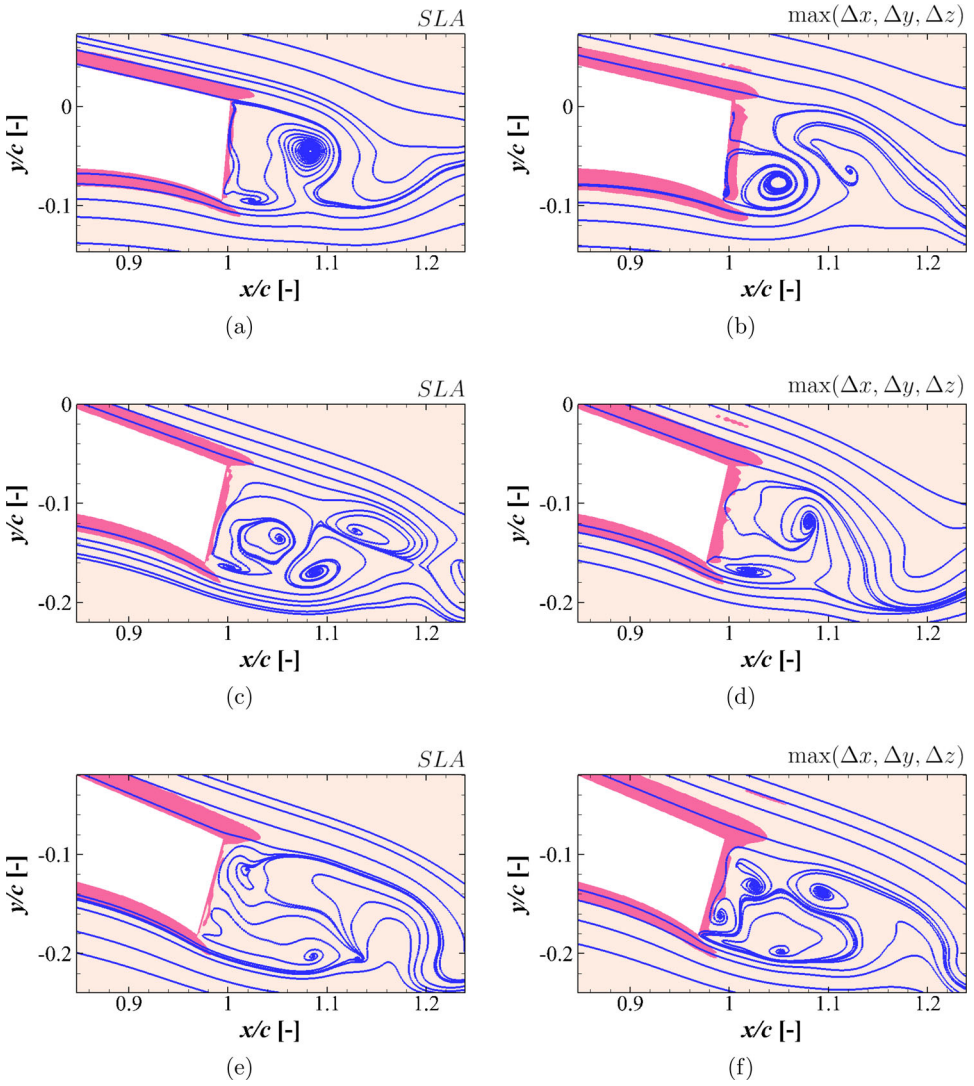

Figure 12. LES-RANS zone division computed using two methods: SLA and max(Δ*x*, Δ*y*, Δ*z*). Magenta colored zone shows the RANS area. Top: $\alpha = 5.1°$, middle: $\alpha = 12.8°$, and bottom: $\alpha = 15.4°$.

the CFD computations employing DDES turbulence model with SLA method for the DES length scale calculations, except stated otherwise. **Figures 13** and **14** display the vortex structures downstream of the DU 97 W-300 flatback airfoil obtained from three different mesh resolutions and for two turbulence modeling approaches. For easier interpretation of the results, the domain is duplicated three times in spanwise direction for all plots. This is possible because a periodic boundary condition was applied. The wake structures are displayed by quantifying the *Q*-criterion vortex identification in Figure 13 as:

$$Q = \frac{1}{2}\left[(|\boldsymbol{\Omega}|^2 - |\boldsymbol{S}|^2)\right] > 0 \tag{3}$$

with

$$\boldsymbol{\Omega} = \frac{1}{2}[\boldsymbol{\nabla v} - (\boldsymbol{\nabla v})^T] \tag{4}$$

$$\boldsymbol{S} = \frac{1}{2}[\boldsymbol{\nabla v} + (\boldsymbol{\nabla v})^T]. \tag{5}$$

Further visualization of the iso-vorticity is presented in Figure 14 to get a better overview of the case, computed as:

$$\omega_z = \frac{\partial v}{\partial x} - \frac{\partial u}{\partial y}. \tag{6}$$

It can be seen that URANS is unable to generate rich three-dimensional vortex structures as those predicted by DDES in Figures 13 and 14, even when the finest grid resolution is employed. As a result, the vortex shedding predicted by URANS has a strong coherence in spanwise direction which travels downstream. On the other hand, for all considered three-dimensional meshes, DDES-based predictions are characterized by rich vortical structures. As can be seen in Figures 13 and 14, the wake structures are inherently different in terms of the vortex

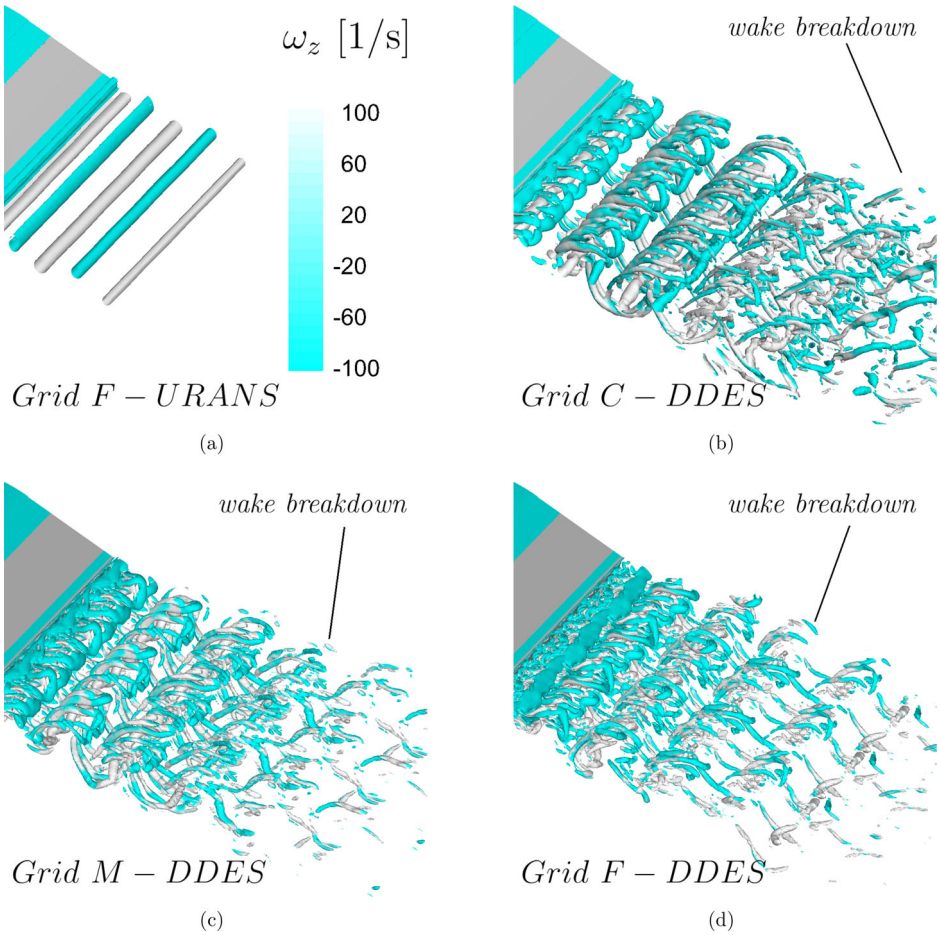

Figure 13. Instantaneous vortex structures ($Q = 200,000 s^{-2}$, at $\alpha = 12.8°$) downstream of the airfoil trailing edge from different mesh resolutions and turbulence modelings colored by the spanwise vorticity. The domain is duplicated three times for visualization purposes.

breakdown. The wake vortex ages faster when a finer mesh resolution is employed. It becomes evident that medium and fine mesh resolutions exhibit earlier wake breakdown than the coarse mesh. The earlier wake breakdown reduces the displacement thickness of the wake flow and yields a reduction in base drag and in the load fluctuations, which have a direct connection with the noise emission. This improves the prediction accuracy and will be discussed in Section 3.1.

To gain deeper insights into the wake characteristics of the flatback airfoil, the mean and statistical parameters are further evaluated based on the DDES results using the fine grid resolution. The flow field is recorded for every time step at several locations (at $x/c = 1.5, 2.0, 2.5, 3.0$ and 3.5) downstream of the airfoil as depicted in **Figure 15**. The results are plotted in **Figure 16** to **Figure** 19.

Figure 16 displays the normalized mean streamwise velocity component downstream of the airfoil trailing edge for three different angles of attack at 5.1°, 12.8°, and 15.4°. The wake centerline (defined as the maximum momentum deficit) changes depending on the angle of the inflow approaching the airfoil. The higher the angle of attack is, the lower the wake centerline is located along y-axis. Note that the angle of attack is changed by rotating the airfoil about its quarter chord location. This wake centerline location is further shifted in negative y direction with increasing streamwise distance. It is interesting to observe that the shift between $\alpha = 5.1°$ to $\alpha = 12.8°$ is much larger than between $\alpha = 12.8°$ to $\alpha = 15.1°$.

The Reynolds normal stress ($\overline{u'u'}$) for three different angles of attack is plotted in **Figure** 17. All considered angles of attack yield a similar Reynolds normal stress profile shape in vertical direction. The Reynolds normal stress starts to increase with increasing momentum deficit on both sides (from positive and negative y directions). It reaches the maximum shortly afterwards, at ≈20% of the half-wake width. This is followed by a reduction in the Reynolds normal stress until it reaches the minimum around the wake centerline itself. This indicates that the mixing process is emanated mainly from the sharp edge of the trailing edge base. Furthermore, the Reynolds normal stress decays very fast with increasing streamwise distance which indicates that the breakdown of the coherent wake structures occurs near the airfoil itself, which is in consistent with the observation made in Figure 13.

The $\overline{u'v'}$ Reynolds stress component for three different angles of attack is plotted in Figure 18. It can be seen that the angle of attack has a stronger influence on this component than on the Reynolds normal stress. The magnitude of $\overline{u'v'}$ increases

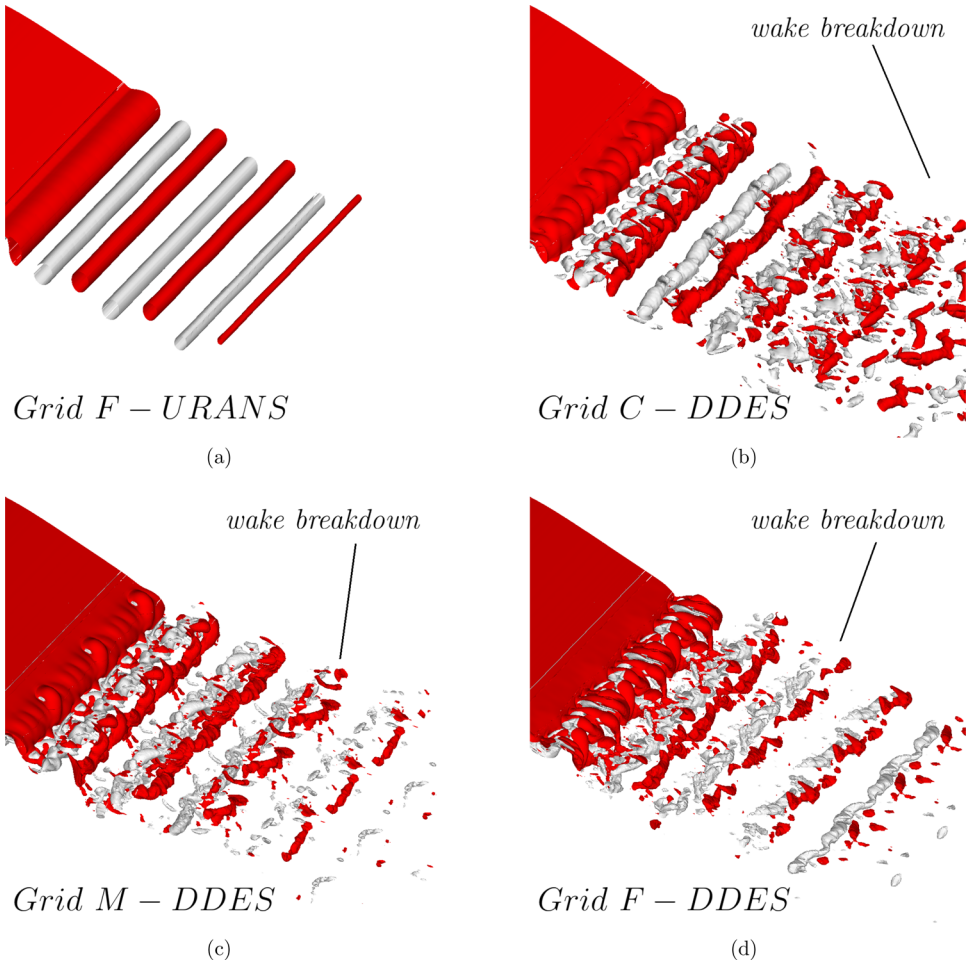

Figure 14. Instantaneous iso-structures of spanwise vorticity at $\omega_z = -400\text{s}^{-1}$ (red) and $\omega_z = 400\text{s}^{-1}$ (gray). DES length scale calculations adopt the SLA approach. The domain is duplicated three times for visualization purposes.

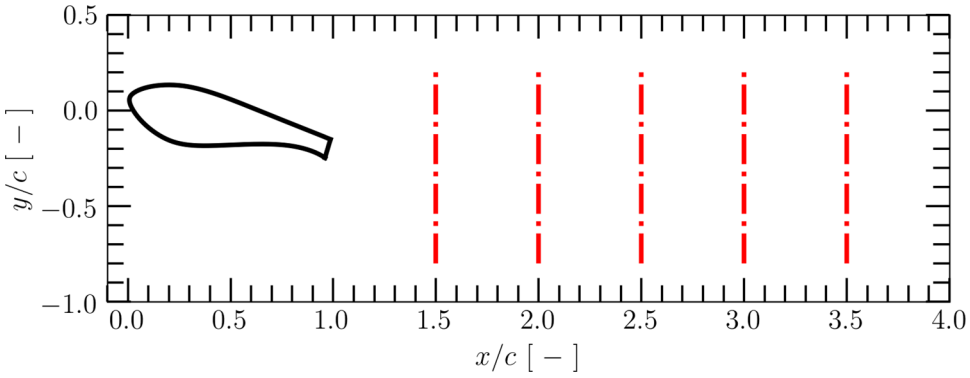

Figure 15. Locations of the wake evaluation downstream of the airfoil (marked by red dash-dotted lines) at $x/c = 1.5$, 2.0, 2.5, 3.0, and 3.5.

considerably high when the angle of attack increases from 5.1° to 12.8° at $x/c = 1.5$. Further increasing streamwise distance causes the difference to be minimal. The higher level of $\overline{u'v'}$ promotes turbulent wake mixing process. In fact, the noise level reduces with increasing angle of attack, both in experiment and in CFD results shown in Figure 11, which seems to be connected. It is expected that modifying this aspect could alter the noise characteristics.

Figure 19 presents the $\overline{u'w'}$ Reynolds stress component for three different angles of attack. The magnitude of the Reynolds stress in this tensor direction is much smaller than the other two investigated components. This could be caused by the strong

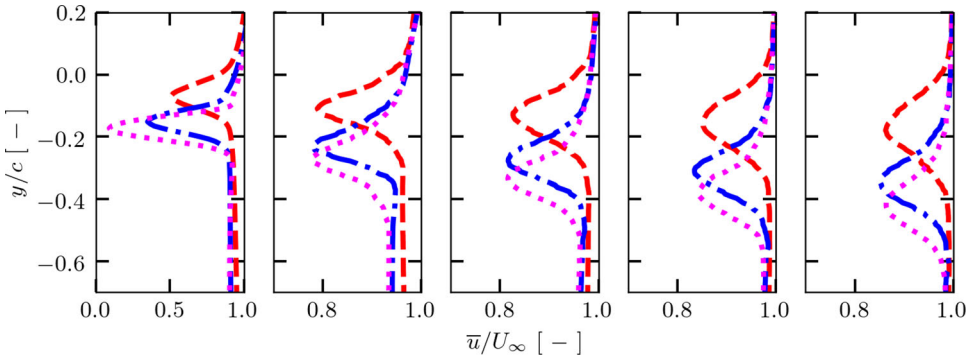

Figure 16. Normalized mean streamwise velocity component downstream of the airfoil trailing edge for three different angles of attack: (a_ _ _) $\alpha = 5.1°$, (b_.._.) $\alpha = 12.8°$, and (c.....) $\alpha = 15.4°$. From left to right: $x/c = 1.5$, 2.0, 2.5, 3.0, and 3.5.

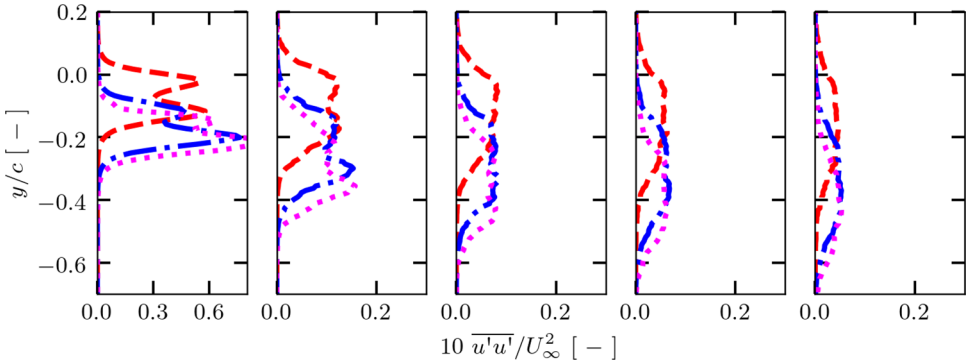

Figure 17. Normalized Reynolds normal stress ($\overline{u'u'}$) downstream of the airfoil trailing edge for three different angles of attack: (a_ _ _) $\alpha = 5.1°$, (b_.._.) $\alpha = 12.8°$, and (c.....) $\alpha = 15.4°$. From left to right: $x/c = 1.5$, 2.0, 2.5, 3.0, and 3.5.

coherence of the vortex structure in spanwise direction. This indicates a small value in the spanwise velocity gradient. As a result, this component has a very small contribution on the drag generation and noise emission. Increasing this Reynolds stress component may change the breakdown of the wake and could possibly improve the aerodynamic and acoustic characteristics.

From the studies, it can be seen that the area near the two end edges of the blunt trailing edge shows the strongest pressure fluctuations among the other parts of the trailing edge, see **Figure 20**. As an implication, the pressure fluctuations are directly represented in the acoustic flow field in **Figure 21**. Altering the pressure characteristics within this area of may help promoting the breakdown of the coherent vortices and ultimately reducing the noise tonality.

3.5. Proper Orthogonal Decomposition

In this section, deeper investigations will be carried out by evaluating the wake flow based on its energy content. The flow field in the wake is highly turbulent and clear analysis is often difficult to be done due to its chaotic nature. Such complex flow

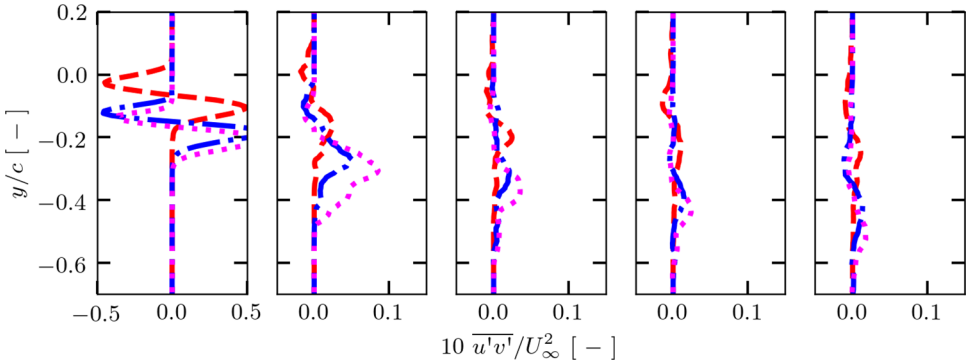

Figure 18. Normalized Reynolds stress component ($\overline{u'v'}$) downstream of the airfoil trailing edge for three different angles of attack: (a_ _ _) $\alpha = 5.1°$, (b_.._.) $\alpha = 12.8°$, and (c.....) $\alpha = 15.4°$. From left to right: $x/c = 1.5$, 2.0, 2.5, 3.0, and 3.5.

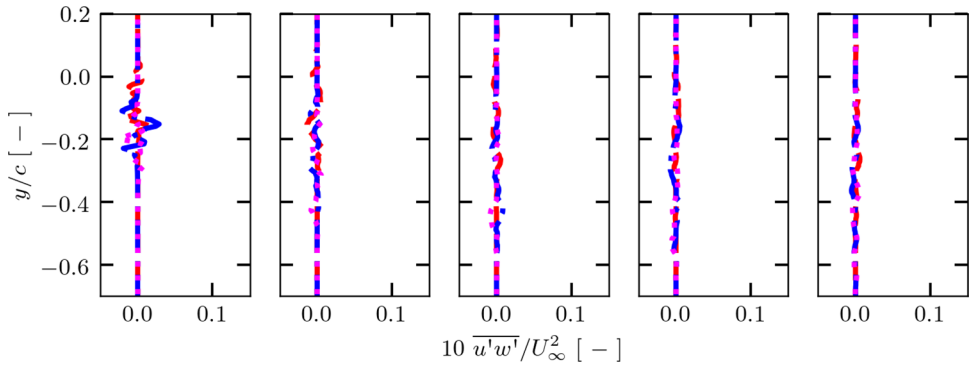

Figure 19. Normalized Reynolds stress component ($\overline{u'w'}$) downstream of the airfoil trailing edge for three different angles of attack: (a_ _ _) $\alpha = 5.1°$, (b_ . _ .) $\alpha = 12.8°$, and (c.....) $\alpha = 15.4°$. From left to right: $x/c = 1.5, 2.0, 2.5, 3.0$, and 3.5.

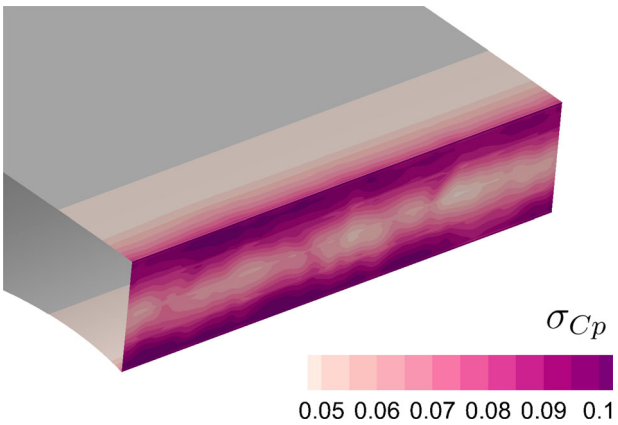

Figure 20. Pressure fluctuations on the airfoil surface near the trailing edge area.

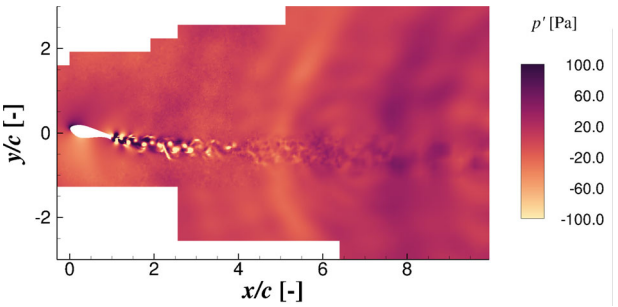

Figure 21. Instantaneous resolved acoustic pressure in the wake of the airfoil.

characteristics are difficult to capture numerically without the usage of high fidelity computations. Many studies have documented the importance of high fidelity modeling in producing good data,[47–54] highlighting the need of eddy resolving approaches for capturing the unsteady fluctuations. Furthermore, to understand the physical mechanisms of the complex flow characteristics, modal decomposition approaches provide a valuable insight into the flow physics since they are able to separate different flow characteristics into different modes. Proper orthogonal decomposition (POD) and dynamic mode decomposition (DMD)

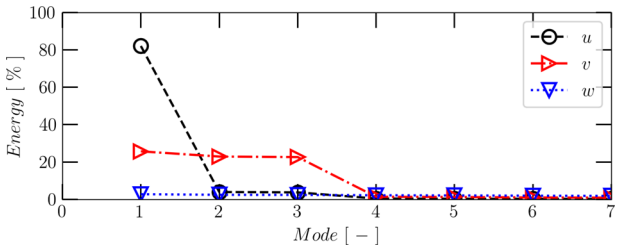

Figure 22. Relative energy content of each mode for three components of velocities in the wake as a function of the POD mode.

are two methods widely used for extracting the dominant modes of the fluid flow. Recently there were also attempts to employ deep neural networks based on autoencoders for achieving the same goal with better flow reconstruction capabilities.[55–58] POD analyses were done in the present studies to extract the dominant flow characteristics. The calculations were carried out employing the snapshot method[59] implemented in the Python package *modred* (https://modred.readthedocs.io). Weiss[60] provided a good overview concerning the usage and derivation of POD for fluid dynamics problems.

Figure 22 displays the relative energy content of the fluid flow in the wake as a function of the POD mode, computed as:

$$Energy = \frac{E_k^{\phi}}{\sum_{k=1}^{N} E_k^{\phi}} \cdot 100\% \approx \frac{\lambda_k^{\phi}}{\sum_{k=1}^{N} \lambda_k^{\phi}} \cdot 100\% \tag{7}$$

with E_k^{ϕ} and λ_k^{ϕ} being the energy content and eigen value of the POD mode k for the evaluated component $\phi \in u, v, w$, respectively, and N being the total identifiable modes. It can be seen that the first mode is highly dominant for the u-component, with more than 80% of the relative energy content for u. For the v-component, the first three modes show relatively comparable significance, then the energy drops for the higher POD modes. Interestingly, the spanwise velocity component (w) shows relatively low energy content even for the first POD mode indicating that the energy is spread out throughout all identifiable POD modes.

Further physical meaning can be derived by evaluating the flow structures of the first three POD modes in **Figure 23**. One can see that the first POD mode of the streamwise velocity is

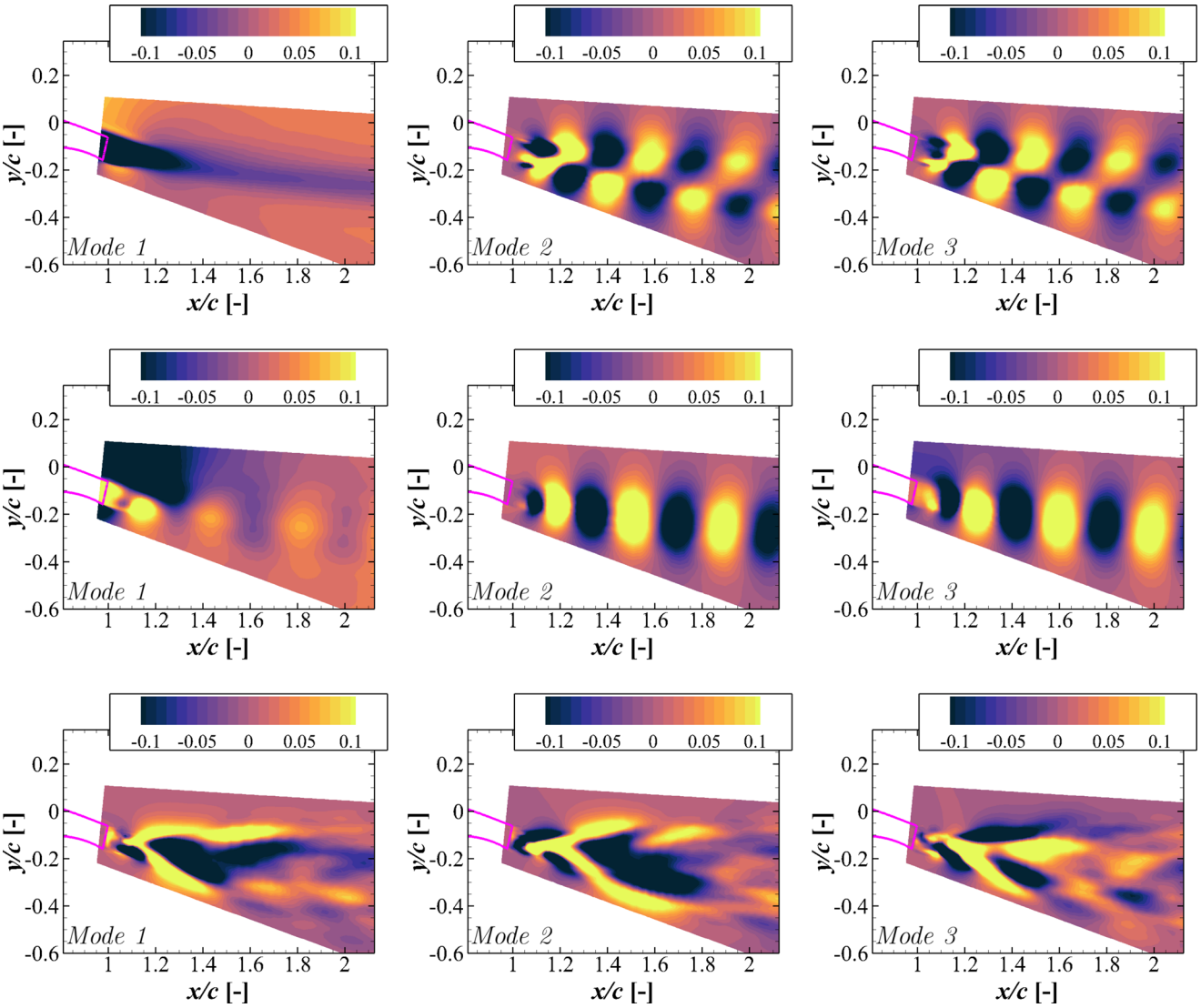

Figure 23. Proper orthogonal decomposition results in the wake region downstream of the airfoil at $z/c = 0.25$ (mid simulation domain). Top: for u-component, middle: for v-component, bottom: for w-component normalized by U_∞. Results are obtained from fine mesh at $\alpha = 12.8°$ using DDES-SLA turbulence model.

inherently dominated by the steady part of the wake flow. The displacement of the wake is clearly observed. The higher POD modes of the streamwise velocity are characterized by typical vortex shedding effects. Similarly, the shedding effects are also observed for the first POD modes for v. The unsteady shedding term of the first POD mode is clearly contributed mainly by the vertical velocity component since the streamwise component is inherently steady. The spanwise velocity component shows no clear signs of the shedding effects. The flow mode is more chaotic and seems to be more related to the noise caused by the small scale turbulence in the wake having low energy content. Therefore, it can be inferred that the vortex-shedding drag and noise emission of the flatback airfoils are mainly caused from the interaction of the vertical velocity fluctuations with the streamwise velocity component.

4. Conclusions

Aerodynamic and acoustic investigations of thick flatback airfoils have been conducted by employing high fidelity computational approaches. The studies were performed on the flatback version of the DU 97 W-300 airfoil at a Reynolds number of 3.2 million considering soiled conditions. The results were validated with measurement data and further assessments on flow characteristics were carried out. The following aspects could be concluded from the present studies:

1) 2D simulation environment overestimates the drag force and noise emission of the airfoil.
2) 3D URANS is not suitable for investigating the noise and drag characteristics of flatback airfoils.

3) The accuracy of DDES computations improves with increasing grid resolution in spanwise direction. A resolution of $\Delta z < 0.0052c$ is recommended.
4) The choice of DES length scale calculation methods is not sensitive for flatback airfoil, where the location of separation is clearly defined by the trailing edge base itself.
5) The improvement of prediction accuracy for the finer mesh resolution is caused by the the improved accuracy in wake structure computations. Wake breakdown occurs earlier for the finer mesh resolution.
6) The Reynolds normal stress ($\overline{u'u'}$) shape is fairly independent of the angle of attack. The mixing process is concentrated near the sharp edge of the trailing edge base.
7) The shape of the $\overline{u'v'}$ Reynolds stress component is dependent on the angle of attack and influence the noise emission.
8) The $\overline{u'w'}$ Reynolds stress component is not significant for flatback airfoils.
9) The surface pressure fluctuations are strongest approaching the two end edges of the blunt trailing edge.
10) POD shows that the interactions between the vertical velocity fluctuations with the streamwise velocity component are the main source of vortex-shedding induced drag and noise emission of flatback airfoils.

Acknowledgements

The authors would gratefully acknowledge the High Performance Computing Center Stuttgart (HLRS) for the computational resources. This research was funded by the German Federal Ministry for Economic Affairs and Energy (BMWi) in the research project IndiAnaWind ("Interdisziplinäre Analyse und Optimierung von Windenergieanlagen und ihrer Komponenten") under grant number 0325719E.

Open access funding enabled and organized by Projekt DEAL.

Conflict of Interest

The authors declare no conflict of interest.

Data Availability Statement

The data that support the findings of this study are available from the corresponding author upon reasonable request.

Keywords

acoustics, aerodynamics, CFD, flatback airfoil, turbulence, wake

Received: February 26, 2022
Revised: April 13, 2022
Published online: May 12, 2022

[1] C. Walsh, Wind energy in europe in 2019 - trends and statistics, Technical report, Wind Europe, **2020**.
[2] L. Castro-Santos, A. F. Vizoso, E. M. Camacho, L. Piegiari, *Energy Sources, Part B: Economics, Planning, and Policy* **2016**, *11*, 974.
[3] G. Bangga, *Three-Dimensional Flow in the Root Region of Wind Turbine Rotors*, Kassel University press GmbH, ISBN: 978-3-7376-0536-6, Kassel University Press, Germany **2018**.
[4] W. Timmer, R. Van Rooij, *J. Sol. Energy Eng.* **2003**, *125*, 488.
[5] R. Van Rooij, W. Timmer, *J. Sol. Energy Eng.* **2003**, *125*, 468.
[6] G. Bangga, T. Kusumadewi, G. Hutomo, A. Sabila, T. Syawitri, H. Setiadi, M. Faisal, R. Wiranegara, Y. Hendranata, D. Lastomo, et al., *J. Phys.: Conf. Ser.* **2018**, *974*, 012019.
[7] P. Fuglsang, C. Bak, *Wind Energy: An Int. J. Prog. Appl. Wind Power Conversion Technol.* **2004**, *7*, 145.
[8] L. Zhang, X. Li, K. Yang, D. Xue, *J. Wind Eng. Ind. Aerodynamics* **2016**, *156*, 84.
[9] J. Herrmann, G. Bangga, *J. Renewable Sustainable Energy* **2019**, *11*, 043304.
[10] R. S. Ehrmann, B. Wilcox, E. B. White, D. C. Maniaci, Effect of surface roughness on wind turbine performance, Technical report, Sandia National Lab.(SNL-NM), Albuquerque, NM (United States), **2017**.
[11] P. Kankatala, G. Bangga, *Adv. Theor. Simul.* **2019**, *2*, 1900077.
[12] B. J. Wilcox, E. B. White, D. C. Maniaci, *Albuquerque, NM* **2017**.
[13] G. Bangga, T. Lutz, E. Krämer, *J. Phys.: Conf. Ser.* **2018**, *1037*, 022025.
[14] M. Miller, K. Lee Slew, E. Matida, *Wind Energy* **2018**, *21*, 1372.
[15] M. Doosttalab, O. Frommann, *AIAA J.* **2019**, *57*, 4639.
[16] K. Standish, C. Van Dam, *J. Sol. Energy Eng.* **2003**, *125*, 479.
[17] J. Baker, E. Mayda, C. Van Dam, **2006**.
[18] G. Papadakis, M. Manolesos, *Wind Energy Sci.* **2020**, *5*, 911.
[19] G. Wang, L. Zhang, W. Z. Shen, *Energy* **2018**, *158*, 911.
[20] G. Bangga, T. Lutz, E. Krämer, In *German Wind Energy Conference 12, DEWEK 2015*, **2015**.
[21] M. F. Barone, D. E. Berg, W. J. Devenport, R. A. Burdisso, Aerodynamic and aeroacoustic tests of a flatback version of the du97-w-300 airfoil, Technical report, Sandia National Lab.(SNL-NM), Albuquerque, NM (United States); Virginia ..., **2009**.
[22] S. Wagner, R. Bareiss, G. Guidati, *Wind Turbine Noise*, Springer Science & Business Media, **2012**.
[23] C. Stone, M. Barone, M. Smith, E. Lynch, In *47th AIAA Aerospace Sciences Meeting including The New Horizons Forum and Aerospace Exposition*, **2009**, 273.
[24] D. Berg, J. Zayas, In *46th AIAA aerospace sciences meeting and exhibit* **2008**, 1455.
[25] J.-H. Jeong, S.-H. Kim, *J. Mech. Sci. Technol.* **2018**, *32*, 2089.
[26] X. Li, K. Yang, H. Hu, X. Wang, S. Kang, *Energies* **2019**, *12*, 270.
[27] H. Shin, H. Kim, T. Kim, S.-H. Kim, S. Lee, Y.-J. Baik, G. Lee, *Energies* **2017**, *10*, 872.
[28] N. Kroll, C.-C. Rossow, K. Becker, F. Thiele, *Aerosp. Sci. Technol.* **2000**, *4*, 223.
[29] P. Weihing, J. Letzgus, G. Bangga, T. Lutz, E. Krämer, In *Symposium on Hybrid RANS-LES Methods*, Springer, **2016**, 369.
[30] U. Kowarsch, M. Keßler, E. Krämer **2013**.
[31] G. Bangga, T. Lutz, *Energy* **2021**, *223*, 120076.
[32] P. Aumann, W. Bartelheimer, H. Bleecke, M. Kuntz, J. Lieser, E. Monsen, B. Eisfeld, J. Fassbender, R. Heinrich, N. Kroll, M. Mauss, J. Raddatz, U. Reisch, B. Roll, T. Schwarz, *FLOWer Installation and User Manual*, Deutsches Zentrum fur Luft- und Raumfahrt, 1 edition, **2008**.
[33] A. Jameson, *AIAA paper* **1991**, *1596*, 1991.
[34] G. Bangga, T. Lutz, In *CadenceLIVE Europe 2021*, **2021**.
[35] X.-D. Liu, S. Osher, T. Chan, *J. Comput. Phys.* **1994**, *115*, 200.
[36] J. Qiu, C.-W. Shu, *J. Comput. Phys.* **2002**, *183*, 187.
[37] D. Levy, G. Puppo, G. Russo, *SIAM J. Sci. Comput.* **2002**, *24*, 480.
[38] G. Capdeville, *J. Comput. Phys.* **2008**, *227*, 2977.
[39] Y. Kim, P. Weihing, C. Schulz, T. Lutz, *J. Wind Eng. Ind. Aerodyn.* **2016**, *156*, 41.
[40] U. Kowarsch, C. Öhrle, M. Keßler, E. Krämer, *J. Am. Helicopter Soc.* **2016**, *61*, 1.
[41] J. Letzgus, P. Weihing, M. Keßler, E. Krämer, In *Progress in Hybrid RANS-LES Modelling*, 311–321. Springer, **2020**.
[42] F. R. Menter, *AIAA journal* **1994**, *32*, 1598.
[43] M. L. Shur, P. R. Spalart, M. K. Strelets, A. K. Travin, *Flow, turbulence and combustion* **2015**, *95*, 709.

[44] A. Wray **1997**.
[45] M. Kessler, S. Wagner, *Computers & fluids* **2004**, *33*, 791.
[46] A. Dessoky, G. Bangga, T. Lutz, E. Krämer, *Energy* **2019**, *175*, 76.
[47] K. Asada, S. Kawai, *Phys. Fluids* **2018**, *30*, 085103.
[48] I. Mary, P. Sagaut, *AIAA J.* **2002**, *40*, 1139.
[49] M. Shur, P. Spalart, M. Strelets, A. Travin, In *Engineering Turbulence Modelling and Experiments 4*, 669–678. Elsevier, **1999**.
[50] Y. Zhang, H. Chen, K. Wang, M. Wang, *AIAA J.* **2017**, *55*, 4219.
[51] H.-J. Kim, S. Lee, N. Fujisawa, *Int. J. Heat Fluid Flow* **2006**, *27*, 229.
[52] A. Frère, K. Hillewaert, P. Chatelain, G. Winckelmans, *Flow, Turbulence and Combustion* **2018**, *101*, 457.
[53] G. Papadakis, M. Manolesos, K. Diakakis, V. A. Riziotis, In *Journal of Physics: Conference Series*, volume *1618*. IOP Publishing, **2020**, 052062.
[54] J. Liu, W. Zhu, Z. Xiao, In *Progress in Hybrid RANS-LES Modelling*, *237*, Springer, **2020**.
[55] G. E. Hinton, R. R. Salakhutdinov, *science* **2006**, *313*, 504.
[56] M. Milano, P. Koumoutsakos, *J. Comput. Phys.* **2002**, *182*, 1.
[57] H. Eivazi, H. Veisi, M. H. Naderi, V. Esfahanian, *Phys. Fluids* **2020**, *32*, 105104.
[58] H. Eivazi, S. L. Clainche, S. Hoyas, R. Vinuesa, *arXiv preprint arXiv:2109.01514* **2021**.
[59] P. Holmes, J. L. Lumley, G. Berkooz, C. W. Rowley, *Turbulence, Coherent Structures, Dynamical Systems and Symmetry*, Cambridge university press, **2012**.
[60] J. Weiss, In *AIAA Aviation 2019 Forum*, **2019**, 3333.